Dalton Transactions

ROYAL SOCIETY OF CHEMISTRY

PAPER

View Article Online
View Journal | View Issue

Cite this: *Dalton Trans.*, 2026, **55**, 4085

Heterometallic incorporation to promote the catalytic activity of polyoxoniobate toward selective oxidation of 5-hydroxymethylfurfural

Li-xiao Song, Zi-wei Cai, Cai-li Lv, Long-fei Chao, Yun-dong Cao,* Wen-jing Xu, Hong Liu,* Chun-hui Zhang and Guang-gang Gao *

5-Hydroxymethylfurfural (HMF) serves as a key platform compound for the production of value-added chemicals from biomass. Consequently, its catalytic oxidation to 2,5-furandicarboxylic acid (FDCA), a highly promising renewable monomer substance, is of particular importance. But this process entails a complex dehydroxylation reaction, which can lead to numerous competing side reactions. Therefore, developing highly selective catalysts for this transformation remains a critical challenge. This study pioneers the use of a polyoxoniobate (PONb) incorporating vanadium and copper amine complexes, $Nb_{12}V_3Cu$, for the catalytic oxidation of HMF. Unlike conventional polyoxometalates (POMs), this PONb-based catalyst exhibits superior stability under alkaline reaction conditions. Comparative experiments reveal that incorporating hetero-metallic components into PONb anions promotes the catalytic centers at the terminal or bridging oxygen atoms. These sites demonstrate enhanced synergistic catalysis towards both the hydroxyl and adjacent methylene groups in HMF, thereby facilitating the dehydrogenation and oxidation processes. Under the optimized conditions, the $Nb_{12}V_3Cu$ catalyst achieved 90.3% HMF conversion with 81.4% FDCA yield, outperforming most reported counterparts, and maintained its activity over five consecutive cycles. This research presents a novel hetero-metallic incorporation approach for the design of polyoxometalate-based catalysts specifically customized for biomass conversion in alkaline media, establishing a robust pathway for cutting-edge research on the selective oxidation of HMF to produce its derived platform chemicals.

Received 27th December 2025,
Accepted 3rd February 2026

DOI: 10.1039/d5dt03085d

rsc.li/dalton

1. Introduction

The inherent conflict between rapid global economic development and the finite supply of fossil resources has established biomass as a critical alternative carbon source for the chemical and petrochemical industries.[1–3] Among various biomass-derived compounds, 2,5-furandicarboxylic acid (FDCA), produced from the catalytic oxidation of 5-hydroxymethylfurfural (HMF), is recognized as one of the twelve most valuable platform chemicals.[4,5] FDCA is a promising candidate for a wide range of industrial applications, notably as a bio-based substitute for terephthalic acid in the synthesis of polymers such as polyesters, polyamides and polyurethanes.[6] For example, its condensation with diamines yields bio-based polyamides (PAs), which are suitable for use in textiles and engineering plastics.[7,8] Additionally, FDCA serves as a key intermediate in pharmaceutical synthesis, contributing to the production of diverse drug molecules, including anti-inflammatory and anti-tumor agents.[9] Current technical pathways for the catalytic oxidation of HMF to FDCA include biological enzymatic,[10] electrocatalytic,[11] photocatalytic,[12,13] and thermocatalytic[14] methods. Among these, thermocatalysis offers distinct advantages for practical industrial groups,[16] which activates the aldehyde hydrogen atoms in HMF and its intermediate DFF, thereby lowering the apparent activation energy and facilitating the overall oxidation.[17,18] It is noteworthy that an acidic catalytic environment tends to promote the hydration of HMF, leading primarily to levulinic acid (LA) and formic acid (FA).[15]

In contrast, alkaline conditions favor the selective oxidation of HMF to FDCA.[15] Alkaline additives provide hydroxyl groups,[16] which activate the aldehyde hydrogen atoms in HMF and its intermediate DFF, thereby lowering the apparent activation energy and facilitating the overall oxidation.[17,18] Additionally, FDCA's low solubility in conventional media is improved under alkaline conditions (*e.g.*, with NaOH,[19] $NaHCO_3$,[20] Na_2CO_3,[21] or $KHCO_3$ [22]) through ionization into soluble salts, enhancing mass transfer and promoting FDCA formation. However, excessively high pH or alkali loading can

School of Materials Science and Engineering, University of Jinan, Jinan 250022, China. E-mail: mse_caoyd@ujn.edu.cn, mse_liuh@ujn.edu.cn, mse_gaogg@ujn.edu.cn

lead to side reactions such as furan ring opening[23] and carbon chain degradation[19] and may accelerate corrosion of catalytic sites and reactor materials.

Although noble metal catalysts (*e.g.*, Au, Ag, Pd, Ru) exhibit high catalytic activity, their large-scale industrial deployment faces significant challenges, including scarcity, high cost, and deactivation issues in alkaline media, such as metal leaching, active site degradation, and structural corrosion.[20–26] Polyoxometalates (POMs),[27–29] a class of metal–oxygen clusters comprising high-valence transition metals (*e.g.*, V, Mo, W) linked by bridging oxygen atoms, offer distinct advantages such as tunable structures, diverse compositions,[30–32] high thermal stability,[33,34] and unique redox properties.[35–37] Owing to these characteristics, POMs demonstrate considerable potential for advanced applications, including pharmaceutical synthesis,[38,39] advanced magnetic materials,[40] photochromic materials,[41,42] gas sensors,[43–45] and energy conversion-storage technologies.[46–48] In biomass catalytic conversion, POMs have been demonstrated to effectively convert biomass platform molecules like HMF into high-value chemicals, including DFF[49–52] and FDCA.[53,54] Recent studies indicate that vanadium-substituted Keggin-type phosphomolybdates[53] and organo-ligand-modified polyoxomolybdates[54] can significantly enhance the catalytic efficiency of HMF oxidation to FDCA.

Most FDCA catalytic systems require alkaline additives, whereas conventional POMs maintain structural integrity only under acidic conditions. This incompatibility often leads to the structural collapse of POM frameworks and leaching of active components, preventing catalyst reuse. Consequently, developing novel POM-based catalysts that concurrently demonstrate high activity, robust stability under alkaline conditions, and low cost is of considerable scientific and practical importance. Among diverse POMs, polyoxoniobates (PONbs) are notable for their stability in alkaline media. Their structural features, including high charge density and specific surface area, underpin potential applications in virology,[55] catalysis, and degradation processes.[56–58] In biomass catalysis, PONbs are commonly employed in reactions such as dehydrogenation and lignin cleavage.[57,59,60] Unlike POMs based on tungsten, molybdenum, or vanadium, the Nb^{5+} centers in PONbs are not readily reducible, conferring high structural stability.[59,62] Consequently, their high charge density enables them to catalyze reactions by adsorbing and activating polar terminal hydrogen atoms on organic substrates. Reported studies suggest that PONbs typically operate synergistically with redox-active transition metals (*e.g.*, Co, Cu, or Zr). In such catalytic systems, PONbs activate substrates by adsorbing terminal hydrogen atoms, while the transition metal ions serve as redox centers to accelerate substrate conversion.[61,62] Previous studies have shown that in the Nb_6 structure, adjacent terminal oxygen (O_t) and bridging oxygen (O_b) sites can synergistically activate the C_β–H bond of the PP-monomer. Subsequently, molecular oxygen is inserted, followed by Cu/C_3N_4-catalyzed selective cleavage of the C_α–C_β bond, ultimately yielding high-value aromatic products. DFT calculations reveal that a similar O_t/O_b synergistic activation mechanism also operates during the oxidation of HMF: these dual sites can concurrently initiate the activation of the hydroxyl group and the adjacent C–H bond, thereby promoting the oxidation reaction.

In previous studies on the base-mediated oxidation of HMF, PONbs exhibited relatively weak redox activity. Unlike the composite system PONb-Co/Cu, $Nb_{12}V_3Cu$ is a single-component material that combines good stability and high catalytic activity in the oxidation of HMF, while also allowing systematic theoretical calculations and mechanistic investigations at the molecular level. Building on the aforementioned insights, this work systematically evaluates the catalytic performance of stable PONbs for HMF oxidation under alkaline conditions, resulting in the identification of an efficient PONb catalyst comprising a copper complex and vanadium-substituted component. This ternary catalytic system markedly enhanced the HMF oxidation efficiency through synergistic interactions among its components. Under the optimized conditions, this catalyst achieves efficient conversion of HMF to FDCA, affording a conversion rate of 90.3% and a selectivity of 90.14%, significantly surpassing the performance of most reported catalysts.

2. Results and discussion

In the research on the pathway for converting HMF to FDCA using POMs as a catalyst (Fig. S1), the primary structural types employed include Keggin-type phosphomolybdates and their vanadium-substituted derivatives, as well as POMs by organic cations (Table S1, index 2). Representative catalysts include $H_3[PMo_{12}O_{40}]$, $H_4[PMo_{11}VO_{40}]$, $H_5[PMo_{10}V_2O_{40}]$, $H_9[PMo_6V_6O_{40}]$, $[EMIM]_4Mo_8O_{26}$, $[CTAB]_4Mo_8O_{26}$, $[EPy]_4Mo_8O_{26}$, *etc.*[53,54] However, in catalytic systems based on polyoxomolybdates, the introduction of basic additives such as NaOH severely compromises their structural stability. Consequently, these catalysts are unsuitable for the recyclable or stable production of FDCA. However, while $H_9[PMo_6V_6O_{40}]$ (PMo_6V_6) exhibits catalytic activity, its reported reactions are conducted in ionic liquid media (Table S1, indexes 6 and 7).[53] The high cost of ionic liquids substantially raises the overall production cost, thereby limiting their practical applicability. Fig. 1 illustrates the two PONbs investigated in this work and their associated catalytic process. $K_7[HNb_6O_{19}]\cdot 13H_2O$ (Nb_6) contains the Lindqvist-type polyoxoanion $[Nb_6O_{19}]^{8-}$, which exhibits a highly symmetric architecture characteristic of the PONbs family. The $[Nb_6O_{19}]^{8-}$ polyoxoanion is constructed from six NbO_6 octahedra that share edges to form a compact, superoctahedral cluster. This anion can be viewed as a dimer of two corner-sharing $[Nb_3O_{13}]$ trimeric subunits,[56] while $[Cu(en)_2]_{3.5}[Cu(en)_2(H_2O)]\{[VNb_{12}O_{40}(VO)_2][Cu(en)_2]\}\cdot 17H_2O$ ($Nb_{12}V_3Cu$, en = ethylenediamine) can be interpreted as being composed of four $[Nb_3O_{13}]$ units, one $\{VO_4\}$ tetrahedron, two $\{VO_5\}$ polyhedra, and one $[Cu(en)_2]^{2+}$ complex.[63] Within this structural configuration, the vanadium sites in two distinct types of VO_x polyhe-

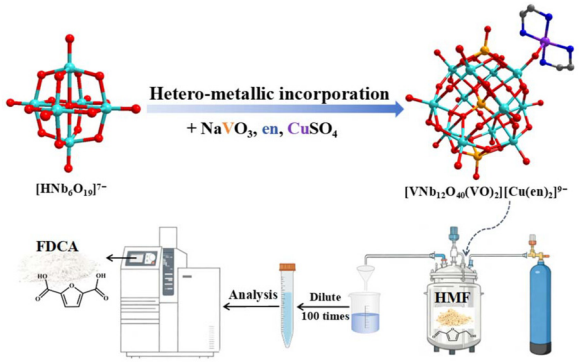

Fig. 1 Schematic illustration of the synthesis of the $Nb_{12}V_3Cu$ and the catalytic detection procedure (color codes: C, grey; N, blue; O, red; Cu, purple; V, yellow; Nb, cyan).

dra adopt differing oxidation states: the central vanadium cation adopts a V^{5+} oxidation state, while the two capping vanadium cations are present as V^{4+}. The ultraviolet-visible diffuse reflectance spectrum (UV-Vis DRS) of $Nb_{12}V_3Cu$ displays distinct absorption bands between 450–900 nm (Fig. S2c), attributable to d–d electron transitions and intervalence charge transfer (IVCT) between V^{4+} and V^{5+}. In contrast, Nb_6 exhibits only a narrow absorption band centered at 250 nm (Fig. S2). The Fourier transform infrared spectrum (FTIR) confirms the successful synthesis of the catalysts (Fig. S3).

The positions and shapes of all characteristic absorption peaks in the spectrum are consistent with the target structure. Additionally, the powder X-ray diffraction (PXRD) patterns (Fig. S4) and Raman spectra (Fig. S5) demonstrate that all three catalysts possess well crystallized structures and exhibit high phase purity. The Mulliken atomic charges and bond lengths for Nb_6 and the structurally optimized $[VNb_{12}(VO)_2]^{11-}$ clusters (without copper–ammonia complexes) are presented in Fig. 2a, b and Fig. S6a, b, respectively. Computational results reveal that bridge oxygen (O_b) exhibits a higher electron cloud density compared to terminal oxygen (O_t) in the PONbs. Therefore, protonation of O_b sites is more favorable than that of O_t sites, which aligns with previously reported findings.[62] After insertion of V, similarly, the O_b site possesses a superior capacity for proton adsorption compared to the O_t site.

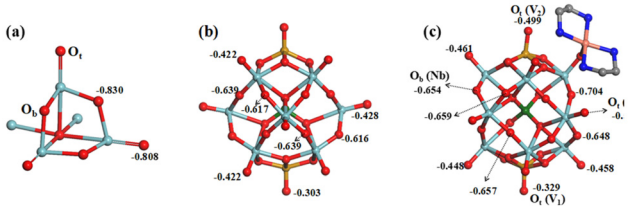

Fig. 2 Mulliken population atomic charges of O_b and O_t in Nb_6 (a), $[VNb_{12}(VO)_2]^{11-}$ (b), and $Nb_{12}V_3Cu$ (c) (some oxygen atoms were omitted for clarity; color codes: C, grey; N, blue; O, red; Cu, orange; V, yellow or green; Nb, cyan).

Moreover, oxygen atoms within the $\{NbO_6\}$ units exhibit higher charge densities compared to those in the $\{VO_5\}$ units, which can be attributed to the differences in the radius and electronegativity between the Nb and V atoms. The coordination of $[Cu(en)_2]^{2+}$ introduces notable alterations in the atomic charges and bond lengths. As depicted in Fig. 2c and Fig. S6c, compared to the $[VNb_{12}(VO)_2]^{11-}$ cluster, the electron cloud density increases variably across all oxygen sites in the $Nb_{12}V_3Cu$. The incorporation of the copper complex elongates the bond lengths within the PONbs framework, thereby modulating the atomic charge distribution and enhancing the proton adsorption capacity of all oxygen sites. Hirshfeld charge (Fig. S6d and e) analysis also leads to the same conclusion: the introduction of the copper complex alters the electron density distribution on the surface, thereby enhancing its proton adsorption and activation capabilities.

The external standard method was employed to quantitatively analyze the contents of HMF, DFF, HMFCA, FFCA, and FDCA during the reaction process (Fig. S7). A systematic evaluation of the catalytic performances of the three catalysts and common vanadate was carried out at 110 °C under 0.8 MPa O_2 (Fig. 3a). Among them, the $Nb_{12}V_3Cu$ catalyst exhibited the highest catalytic oxidation activity. When conventional $NaVO_4$ was used as the catalyst, the HMF conversion reached only 60.02%, with an FDCA yield of 18.58%. For comparison, the reference catalyst Nb_6 was first evaluated alongside Cu

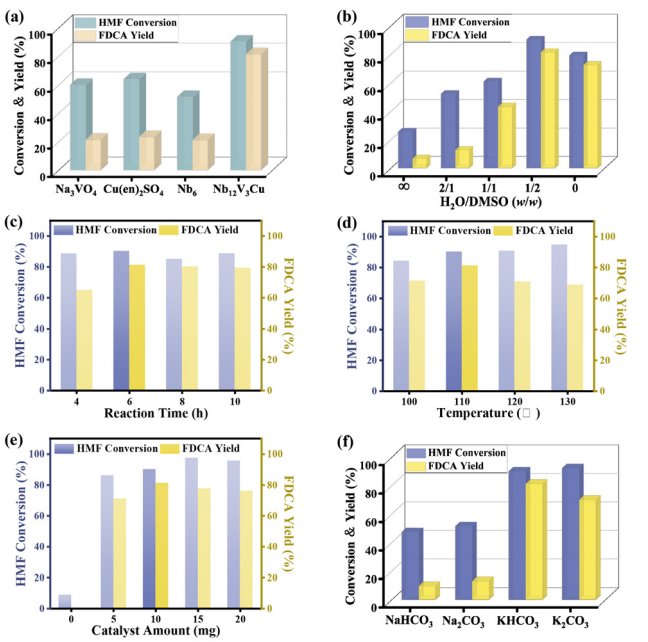

Fig. 3 Catalytic oxidation performance of various catalysts for HMF conversion (a). Reaction conditions: HMF (40 mg), catalyst (10 mg), $KHCO_3$ (70 mg), 110 °C, 6 h, O_2 pressure (0.8 MPa), H_2O/DMSO mass ratio = 1 : 3 (6 mL total solvent). Effects of reaction parameters on HMF oxidation over $Nb_{12}V_3Cu$: H_2O/DMSO mass ratio (6 mL total solvent) (b), reaction duration (c), temperature (d), catalyst loading (e), and alkaline additives (f). Reaction conditions: HMF (40 mg), O_2 pressure (0.8 MPa), alkaline additive (70 mg), solvent (6 mL).

$(en)_2SO_4$. Although $Cu(en)_2SO_4$ is known to promote the oxidation of the hydroxyl group in HMF to an aldehyde,[64] it showed lower selectivity toward FDCA than Nb_6. Notably, under identical conditions, $Nb_{12}V_3Cu$ outperformed Nb_6 (Fig. S8), indicating a significant enhancement in overall catalytic performance. The effects of key reaction parameters on the oxidation of HMF catalyzed by $Nb_{12}V_3Cu$ were systematically investigated, including the H_2O/DMSO solvent mass ratio, reaction time, temperature, catalyst loading, and the type of alkaline additive. Four organic solvents were screened to evaluate the performance of $Nb_{12}V_3Cu$ in the catalytic oxidation of HMF (Fig. S9). The results indicate that among acetonitrile (ACN), ethylene glycol (EG), dimethyl sulfoxide (DMSO), and *N*,*N*-dimethylformamide (DMF), the catalyst exhibited the highest catalytic activity in the DMSO system. This can likely be attributed to the relatively high solubility of FDCA in DMSO, which facilitates product desorption from the catalyst surface and thus promotes the forward reaction. The H_2O/DMSO mass ratio markedly influenced the catalytic performance (Fig. 3b). Utilization of pure water as the reaction medium resulted in suboptimal catalytic efficiency. Both HMF conversion and FDCA yield gradually increased with higher proportions of DMSO. This trend can be attributed to the higher polarity, elevated boiling point, and superior FDCA solubility of DMSO. Specifically, DMSO facilitates the dissolution of FDCA at concentrations up to 30.7 wt%, representing a 256-fold increase compared to the maximum solubility of 0.12 wt% observed in aqueous solutions.[65]

Moreover, the base requirement correlates with water content: although a higher water content enhances the solubility of the base, it may simultaneously increase the medium's alkalinity, thereby promoting HMF degradation. On the other hand, DMSO interacts strongly with the intermediate DFF,[66,67] facilitating its formation and stabilization. However, this strong interaction may also arrest the oxidation at the DFF stage, which suppresses the formation of downstream intermediates like 2,5-furandicarboxylic acid (FFCA) and ultimately hinders the accumulation of the final product, FDCA. This effect accounts for the observed performance decline at excessively high DMSO content.

Additionally, DMSO enhances oxygen dissolution in the reaction system, which further accelerates the overall oxidation process.[68] The FDCA yield and HMF conversion reached their maximum values at a reaction time of 6 hours (Fig. 3c). Fig. 3d indicates that the reaction temperature was positively correlated with the HMF conversion rate. The FDCA yield initially increased with temperature but decreased upon further heating beyond an optimum point. This trend can be explained by the enhanced activation of substrate molecules and improved contact with catalytic active sites at elevated temperatures. However, when the reaction temperature was further raised to 120 °C and 130 °C, the FDCA yield decreased markedly, which can be attributed to the thermal decomposition of FDCA and the propensity of HMF to undergo polymerization or degradation into humic substances.[53] At catalyst loadings of 15 mg and 20 mg (Fig. 3e), the selectivity toward FDCA decreased significantly, possibly due to increased formation of other by-products in the reaction system. Furthermore, alkaline additives promote FDCA formation, as OH^- facilitates the stepwise oxidation of aldehyde groups in HMF to carboxyl groups *via* nucleophilic action.[56] When NaOH and KOH were used as alkaline additives, although HMF conversion was nearly complete, the selectivity toward FDCA remained low (Fig. S10), indicating the occurrence of side reactions under strong alkaline conditions. Therefore, a milder alkali was selected for the subsequent experiments. The performance of various alkaline additives, including $NaHCO_3$, Na_2CO_3, $KHCO_3$, and K_2CO_3, was systematically evaluated (Fig. 3f). The oxidation of HMF shows a strong dependence on the alkali type: HMF conversion followed the order $KHCO_3 \approx K_2CO_3 > NaHCO_3 \approx Na_2CO_3$, whereas the FDCA yield decreases in the sequence $KHCO_3 > K_2CO_3 > NaHCO_3 \approx Na_2CO_3$. The optimal dosage of $KHCO_3$ was investigated (Fig. S11). The $Nb_{12}V_3Cu$ catalyst exhibited optimal performance for HMF oxidation when 70 mg of $KHCO_3$ was added. Further increasing the base amount led to a gradual decline in FDCA yield, which may be attributed to the nonselective decomposition of HMF and a decrease in FDCA selectivity induced by excess alkali. This phenomenon can be attributed to the tendency of DMSO to induce side reactions of furan products in the presence of excess alkali. Among the screened bases, $KHCO_3$ exhibits moderate alkalinity and induced the least furan-related side reactions within the $Nb_{12}V_3Cu$ catalytic system. Therefore, $KHCO_3$ was identified as the optimal alkaline additive for maximizing FDCA production while suppressing undesired side reactions. Compared with other catalysts reported in the literature, $Nb_{12}V_3Cu$ demonstrated superior catalytic activity for HMF oxidation. Under a high HMF-to-catalyst (HMF/cat.) ratio, this system achieved 90.3% HMF conversion and 81.4% FDCA yield.

The kinetic behavior of the HMF oxidation reaction was evaluated by determining the apparent activation energy (Fig. S12). Based on the Arrhenius graph in Fig. 4a, the apparent activation energy (E_a) for $Cu(en)_2SO_4$, Nb_6, and $Nb_{12}V_3Cu$ was calculated to be 64.5 kJ mol^{-1}, 52.8 kJ mol^{-1}, and 44.8 kJ mol^{-1}, respectively. The differences in E_a and observed reaction rates reflect the variations in the frequency factor (A) among the three catalysts. The cyclic voltammetry (CV) test curve shown in Fig. 4b revealed initial oxidation potentials of −0.05 V for $Cu(en)_2SO_4$ and +0.08 V for $Nb_{12}V_3Cu$, while no distinct oxidation signal was detected for Na_3VO_4 and Nb_6. These electrochemical results suggest that $Nb_{12}V_3Cu$ possesses the most favorable oxidation catalytic performance. It is also noteworthy that, compared to heterogeneous systems, homogeneous catalytic reactions face the inherent challenge of catalyst separation and recycling. To enable efficient catalyst reuse, homogeneous catalysts must retain high activity, selectivity, and structural integrity even at elevated product concentrations. The operational stability of $Nb_{12}V_3Cu$ was assessed *via* batch cycling experiments, in which HMF was added sequentially without isolating the FDCA product. Over five consecutive reaction cycles, $Nb_{12}V_3Cu$ maintained high catalytic

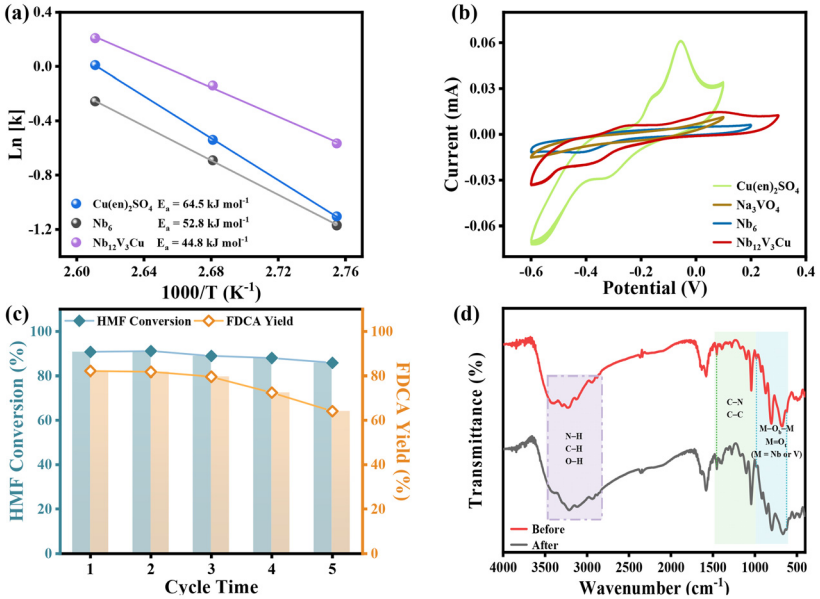

Fig. 4 Activation energy of different catalysts for HMF oxidation (a). The CV curves of $Cu(en)_2SO_4$, Na_3VO_4, Nb_6, and $Nb_{12}V_3Cu$ in $KHCO_3$ solution (0.3 M) (b). Cycle tests for HMF oxidation by $Nb_{12}V_3Cu$ (c). Reaction conditions: HMF (40 mg), catalyst (10 mg), $KHCO_3$ (70 mg), 110 °C, 6 h, O_2 pressure (0.8 MPa), H_2O/DMSO mass ratio = 1 : 3 (6 mL total solvent). FTIR spectra of $Nb_{12}V_3Cu$ before and after the reaction (d).

stability, with a marginal decrease (~5%) in HMF conversion (Fig. 4c). The post-reaction solution was dried, and the resulting solid was sequentially washed with ethanol, centrifuged, and dried again. The mass of the recovered catalyst was approximately 95% of the initial mass. This mass loss may be attributed to the adherence of the sample to the container walls during the drying process and minor losses during centrifugation and transfer. However, the FDCA yield declined by approximately 10% after the fourth cycle. This decrease is likely due to the formation of humic substances from HMF during the reaction,[69–71] which may deposit on the catalyst surface and block active sites, thereby hindering the reactant access and lowering the efficiency. To probe the structural integrity of the catalyst after the reaction, post-reaction characterization was conducted. The transmission electron microscopy (TEM) images of $Nb_{12}V_3Cu$ before and after the reaction (Fig. S13) and UV-Vis DRS after the reaction with $Nb_{12}V_3Cu$ (Fig. S14) provide further insight into its stability. More importantly, FTIR analysis of the spent catalyst (Fig. 4d) indicated that the positions and line shapes of the characteristic absorption peaks remained consistent with those of the fresh $Nb_{12}V_3Cu$ sample. The XRD patterns of the catalyst after cycling (Fig. S15) indicate that its structure and crystal phase remain intact. The corresponding elemental mapping (Fig. S16) further shows that no leaching or loss of copper and vanadium elements occurred. These results collectively confirm that the structural integrity of the catalyst was maintained throughout the catalytic process. Unlike reported POM catalysts, the $Nb_{12}V_3Cu$ catalyst exhibits notable stability under alkaline conditions and maintains high efficacy in the catalytic oxidation of HMF to FDCA over multiple cycles. To elucidate the mechanism of HMF catalytic oxidation, the active site structure was systematically investigated. A control experiment was conducted by replacing O_2 with N_2 under identical solvent and pressure conditions (Fig. 5a). The catalytic performance of Nb_6 remained largely unaffected under these conditions. In contrast, when $Nb_{12}V_3Cu$ was employed as the catalyst, the FDCA yield decreased significantly, indicating that O_2 was the key substance involved in this oxidation reaction.

To further probe the active sites in $Nb_{12}V_3Cu$, catalytic experiments were performed using pyridine as a molecular probe at varying concentrations (Fig. 5b). When the addition amount of pyridine reached 100 μL, HMF conversion decreased to 71% and the FDCA yield dropped to 52%. This suppression of catalytic activity is attributed to the selective adsorption of pyridine onto the Lewis acid site (Cu^{2+}), thereby blocking its catalytic function. Radical quenching experiments were carried out to investigate the reaction pathway (Fig. 5c). Adding quenching agents such as isopropanol (2-PrOH), *p*-benzoquinone (P-BQ), and L-tryptophan, did not significantly alter either the HMF conversion rate or the FDCA yield. These results suggest the absence of conventional radical species, such as superoxide radicals ($^{\bullet}O_2^-$), in the catalytic mechanism. This conclusion is further corroborated by UV-vis analysis, which detected no formation of H_2O_2 during the reaction (Fig. S17). X-ray photoelectron spectroscopy (XPS) was performed on the spent $Nb_{12}V_3Cu$ catalyst under both aerobic and anaerobic conditions to elucidate the redox behavior of its metal centers. As shown in Fig. 5d, the Cu 2p spectrum after the O_2 reaction exhibited peaks at 931.9 eV (for $2p_{3/2}$) and 951.8 eV (for $2p_{1/2}$) corresponding to Cu^+, along with peaks at 933.9 eV and 953.8 eV assigned to Cu^{2+}. Under a N_2 atmosphere, the corresponding binding energies shifted slightly to 931.8/951.7 eV for Cu^+ and 933.8/953.7 eV for Cu^{2+}.[72] Semi-

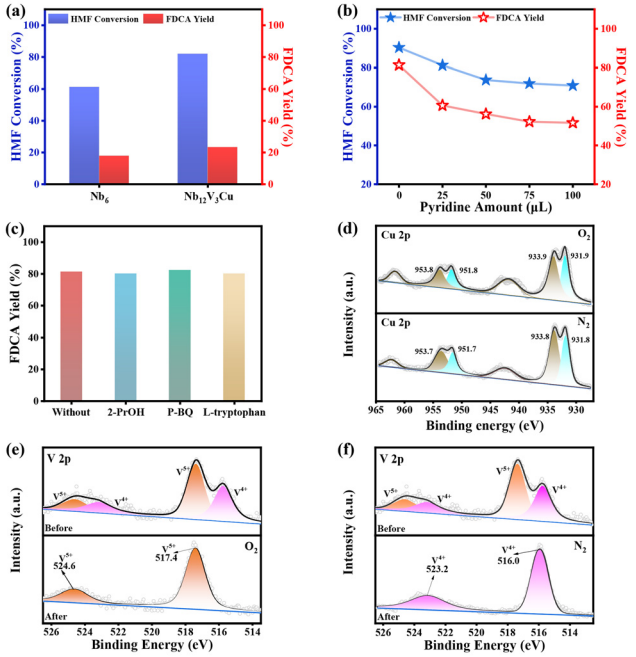

Fig. 5 The catalytic performance of Nb_6 and $Nb_{12}V_3Cu$ in an N_2 atmosphere (a). Pyridine probe experiment for HMF oxidation over $Nb_{12}V_3Cu$ (b). Radical quenching experiments for HMF oxidation over $Nb_{12}V_3Cu$ (c). Reaction conditions: HMF (40 mg), catalyst (10 mg), $KHCO_3$ (70 mg), 110 °C, 6 h, gas pressure (0.8 MPa), H_2O/DMSO mass ratio = 1 : 3 (6 mL total solvent), scavenger (0.25 mmol). Cu 2p XPS analysis of $Nb_{12}V_3Cu$ after reaction under O_2 and N_2 (d). V 2p XPS analyses of $Nb_{12}V_3Cu$ before and after reaction under O_2 (e) and N_2 (f).

quantitative analysis of the XPS peak areas revealed that 45.4% and 46.3% of Cu^{2+} was reduced to Cu^{+} under O_2 and N_2 conditions, respectively, confirming the participation of copper in redox cycling. A similar redox behavior was observed for the reference compound $Cu(en)_2SO_4$ (Fig. S18). In the V 2p region (Fig. 5e and f), only the V^{5+} characteristic peaks (517.4 eV and 524.6 eV) were detected after the reaction under O_2. In contrast, all vanadium species existed as V^{4+} (516.0 eV and 523.2 eV) under N_2.[49] This indicates that when O_2 is present, the reduced state of V^{4+} is re-oxidized to the higher oxidation state of V^{5+}, and V^{5+} continues to participate in the oxidation process of HMF, thereby significantly enhancing the catalytic oxidation performance. Control experiments performed without any catalyst at identical O_2 pressure showed no significant conversion of HMF to FDCA (Fig. S19), demonstrating that O_2 alone cannot directly and selectively oxidize HMF to FDCA, and its oxidation efficiency is extremely low. Furthermore, XPS analysis of the Nb 3d region in both Nb_6 (Fig. S20) and $Nb_{12}V_3Cu$ (Fig. S21) showed no change in the niobium element after the reaction, which once again demonstrates the stability of niobium in the PONbs structure. In summary, O_2 facilitates the redox cycle between Cu^{+}/Cu^{2+} and V^{4+}/V^{5+} during the catalytic conversion process, which significantly accelerates the conversion of HMF to FDCA.

To elucidate the catalytic reaction mechanism, systematic density functional theory (DFT) calculations were performed. As illustrated in Fig. 6a and b, the electron density distribution and electrostatic potential of Nb_6 and $Nb_{12}V_3Cu$ were examined. The results reveal high electron density around the terminal and bridging oxygen atoms in the peripheral $\{VO_5\}$ and $\{NbO_6\}$ coordination polyhedra, suggesting that these sites possess high electronegativity and nucleophilic character toward hydrogen atoms. Frontier orbital analysis of $Nb_{12}V_3Cu$ was subsequently performed to identify potential catalytic sites. As shown in Fig. 6c and d, the highest occupied molecular orbital (HOMO) is primarily localized on the PONb cluster, the sites prone to involvement in electron transfer processes. In contrast, the lowest unoccupied molecular orbital (LUMO) is predominantly located on the $[Cu(en)_2]^{2+}$ cation. Moreover, the LUMO distribution further indicates that Cu serves as the primary electron-accepting site, followed by V as the secondary one. In addition, structural optimization and energy calculations were carried out to model the interaction between the terminal oxygen sites of Nb_6 or $Nb_{12}V_3Cu$ and the terminal hydroxyl groups of HMF (Fig. S22). The results indicate that despite minor differences in the adsorption free energy (E_{ads}) of HMF across various terminal oxygen sites, adsorption remains spontaneous at all sites.

Notably, XPS analysis confirmed that the oxidation state of Nb remained constant. To gain deeper insight into the role of the $\{NbO_6\}$ unit in the catalytic oxidation mechanism, subsequent DFT calculations were performed on various configurations of HMF adsorbed onto the $Nb_{12}V_3Cu$ catalyst. It was found that HMF interacts with the $\{NbO_6\}$ structural unit *via* two distinct binding modes. The first is characterized by –OH adsorption on O_t, resulting in O–H bond activation and C–H bond activation by an adjacent O_b ($Nb_{12}V_3Cu$–Nb–O_t, Fig. 6e). In the second mode, $Nb_{12}V_3Cu$–Nb–O_b (Fig. 6f) features –OH adsorption on O_b, activating the O–H bond while the C–H bond is activated by O_t. Both of these combination modes can simultaneously activate the O–H bond and the C–H bond. In contrast, unlike the $\{NbO_6\}$ unit, HMF binding to $\{VO_5\}$ shows key differences. When –OH binds to O_t (V=O_t), the O–H bond is activated, but the C–H bond activation is mediated solely by an O_t from a neighboring $\{NbO_6\}$ unit, not by the $\{VO_5\}$ itself ($Nb_{12}V_3Cu$–V_1–O_t, Fig. 6g). Similarly, when –OH binds to O_t of V_2, the C–H bond activation occurs by an O_t from a neighboring $\{NbO_6\}$ unit ($Nb_{12}V_3Cu$–V_2–O_t, Fig. 6h). However, the $Nb_{12}V_3Cu$–V_1–O_b mode results in no bond activation (Fig. 6i). Given that the interaction between HMF and the $\{VO_5\}$ unit at V_2 yielded the same non-activating result (Fig. S23), it further supports the conclusion that the $\{NbO_6\}$ unit is a principal active site responsible for O–H and C–H bond activation in the $Nb_{12}V_3Cu$ catalyst. Similarly, no change in the valence state of Nb was observed in the XPS analysis after catalysis with Nb_6. Accordingly, binding models of –OH with O_b and O_t were simulated. In the Nb_6–O_b binding model (Fig. S24), the O–H bond was activated by O_b, while the C–H bond was activated by an adjacent O_t. Likewise, in the Nb_6–O_t binding model (Fig. S25), the O–H and C–H bonds were activated by O_t and an adjacent O_b, respectively. It was further demonstrated that the catalytic oxidation capability of PONbs for HMF originates

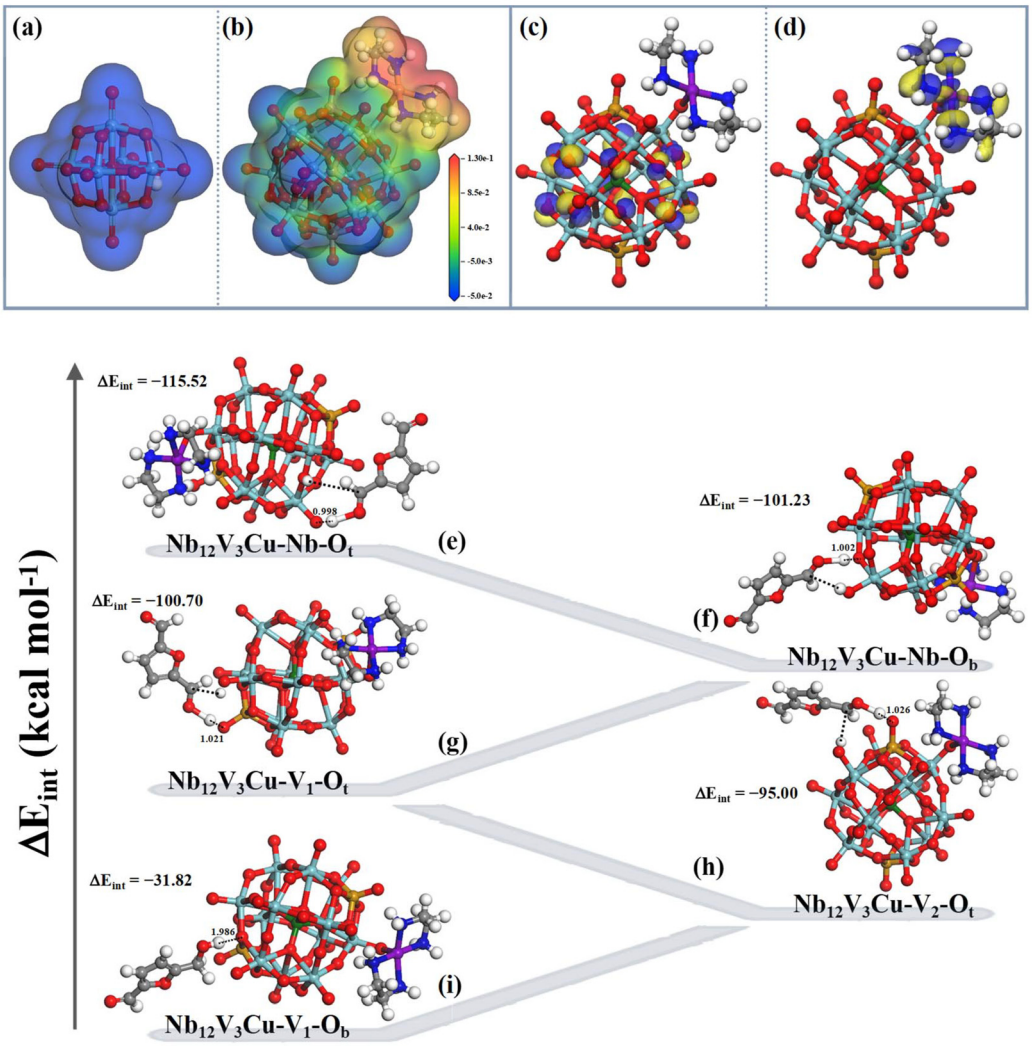

Fig. 6 Electron density maps for Nb_6 (a) and $Nb_{12}V_3Cu$ (b). The frontier orbital analysis of $Nb_{12}V_3Cu$: HOMO (c) and LUMO (d). Structure, interaction energy (ΔE_{int}) and H···O distances (the hydroxyl H atom of HMF and the O atom site of $Nb_{12}V_3Cu$, Å) of the $Nb_{12}V_3Cu$–Nb–O_t (e), $Nb_{12}V_3Cu$–Nb–O_b (f), $Nb_{12}V_3Cu$–V_1–O_t (g), $Nb_{12}V_3Cu$–V_2–O_t (h), and $Nb_{12}V_3Cu$–V_1–O_b (i) binding modes.

from the synergistic activation of O–H and C–H bonds by bridging and terminal oxygen atoms. The interaction energy between the –OH group of HMF and the various O atoms of Nb_6 and $Nb_{12}V_3Cu$ and the bond length variation (Δd) of O–H (Δd_{OH}), C–H (Δd_{CH}), and O–H···O_t (or O_b) distances are shown in Table S2 and Table 1. DFT calculations reveal that compared with the O_t and O_b atoms connected to V, the O_t and O_b atoms related to Nb are more effective in cooperatively activating the O–H and C–H bonds. This cooperative activation facilitates the extraction of protons from HMF, which are transferred to the $Nb_{12}V_3Cu$ catalyst.

Based on XPS analysis and DFT calculations, Cu, V, and Nb in the $Nb_{12}V_3Cu$ catalyst constitute a ternary synergistic catalytic center that facilitates the dehydrogenation and oxidation of HMF and its intermediates. This catalytic conversion involves the directional transfer of electrons and protons, constituting a complete cycle. Furthermore, the unique structure of $Nb_{12}V_3Cu$ provides excellent substrate adsorption performance, enabling the cooperative activation of the –OH and –CH groups. As illustrated in Fig. 7a, the –OH and adjacent –CH

Table 1 The interaction energies between the hydroxyl group of HMF and distinct oxygen species within the $Nb_{12}V_3Cu$ clusters, along with the activated bond length variation (Δd) for O–H (Δd_{OH}), C–H (Δd_{CH}), and H···O distance (specifically H···O_t or H···O_b)

System	ΔE_{int} (kcal mol^{-1})	Δd_{OH} (Å)	Δd_{CH} (Å)	H···O_t (or O_b) (Å)
Nb–O_t	−115.52	0.793	3.261	0.998
Nb–O_b	−101.23	0.748	2.257	0.974
V_1–O_t	−100.70	0.655	2.549	1.021
V_2–O_t	−95.00	0.619	2.891	1.026
V_1–O_b	−31.82	0.035	0.012	1.605
V_2–O_b	−24.23	0.010	0.005	2.368

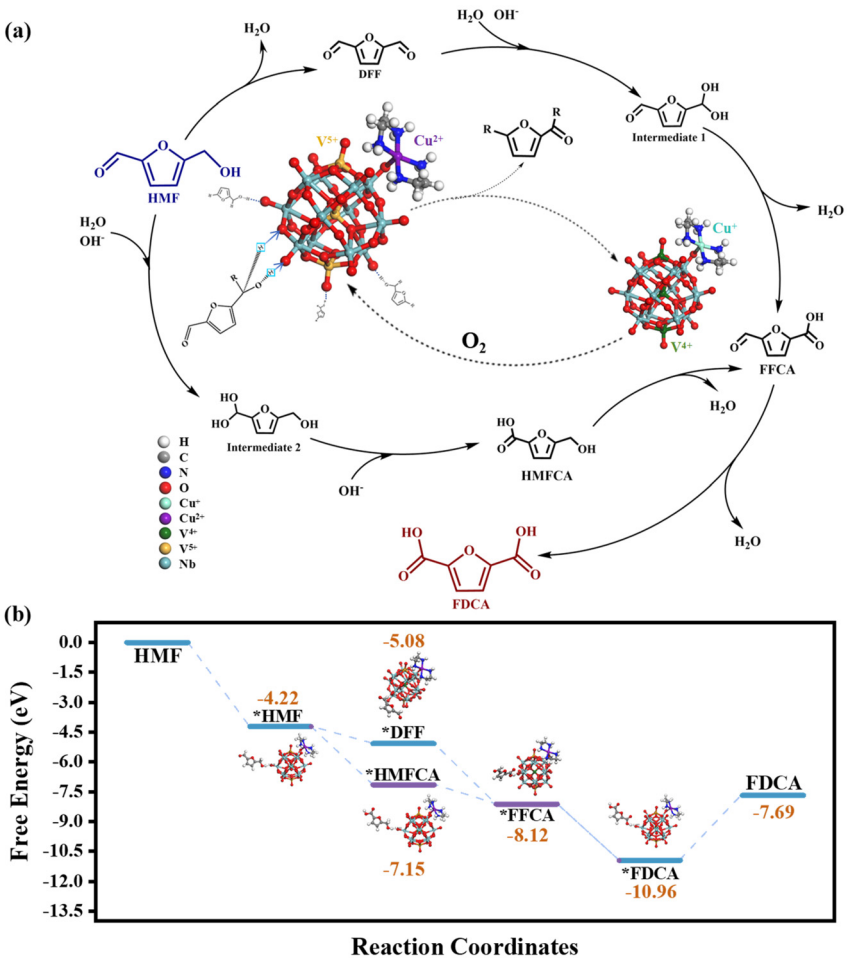

Fig. 7 (a) The proposed catalytic mechanism of $Nb_{12}V_3Cu$ for the conversion of HMF to FDCA. (b) Reaction pathway and the corresponding energy of $Nb_{12}V_3Cu$ in the HMF dehydrogenation/oxygenation process (* represents the adsorption of the corresponding intermediate).

groups of HMF and its reaction intermediates adsorb onto the O_t atom and the neighboring O_b atom of $Nb_{12}V_3Cu$. Subsequently, the O–H and C–H bonds within this group were activated. The protons from both the –CH and –OH groups then transferred to the terminal and adjacent bridging oxygen atoms of the $Nb_{12}V_3Cu$ catalyst. The elimination of these two protons allows the resulting electron-deficient carbon and oxygen atoms to couple, forming a new C=O bond. Concurrently with dehydrogenation, electron transfer occurs from the substrate to the metal centers. Cu^{2+} and V^{5+} act as electron acceptors, being reduced to Cu^{+} and V^{4+}, respectively. Finally, O_2 re-oxidizes these reduced species (Cu^{+} to Cu^{2+} and V^{4+} to V^{5+}), thereby regenerating the catalytic activity and completing the catalytic cycle. The incorporation of heterometallic species (Cu and V) accelerates electron transfer and modulates the electron distribution across the PONb surface, thereby enhancing the overall interaction energy and catalytic efficiency.

Furthermore, the reaction pathways and corresponding relative Gibbs free energy profiles for HMF dehydrogenation/oxidation over the $Nb_{12}V_3Cu$ catalyst were investigated (Fig. 7b). The catalytic oxidation step of HMF on $Nb_{12}V_3Cu$ is shown in Fig. S26. The calculated energy barriers reveal a distinct preference in the reaction itinerary: the conversion of HMF to DFF requires overcoming an energy barrier of −0.86 eV, whereas the pathway toward 5-hydroxymethyl-2-furancarboxylic acid (HMFCA) proceeds with a significantly lower barrier of −2.93 eV. This result indicates that $Nb_{12}V_3Cu$ effectively suppresses kinetic stalling at the stable intermediate DFF, thereby facilitating subsequent reaction steps. In addition, the overall reaction exhibits a monotonic decrease in Gibbs free energy throughout the catalytic cycle. This consistently exergonic profile confirms that the oxidation of HMF is thermodynamically favorable on $Nb_{12}V_3Cu$, underscoring the catalyst's role in driving the reaction forward.

3. Conclusions

In conclusion, this study establishes PONbs as effective catalysts for the oxidation of HMF to FDCA under alkaline conditions. The incorporation of copper and vanadium into the

PONb framework proves to be a pivotal strategy, markedly enhancing the catalytic performance. The optimized catalyst, $Nb_{12}V_3Cu$, effectively combines the inherent HMF adsorption capability of the PONb matrix with the synergistic oxidation activity of V^{5+} and Cu^{2+} sites. Under alkaline conditions, $Nb_{12}V_3Cu$ achieves high HMF conversion, excellent FDCA selectivity, and cycling stability. DFT calculations revealed that the catalytic performance originates from the cooperation between V═O or Nb═O species and bridging oxygen (Nb–O–Nb) pairs, which collectively activate C–H and O–H bonds in HMF. During oxidative processes, proton transfer synchronizes with electron transfer, inducing the reduction of V^{5+} and Cu^{2+} catalytic sites. These reduced centers are subsequently reoxidized by molecular oxygen, thereby regenerating the active catalyst and sustaining catalytic turnover. This work establishes design principles for alkaline POM catalysts: employing stable PONbs, utilizing Nb-centered O_t/O_b pairs for bond activation, and integrating redox heterometals. This framework extends beyond HMF oxidation to biomass valorization, organic C–H functionalization, and energy conversion processes. These findings not only provide a theoretical foundation for the rational design of polyoxometalate catalysts in alkaline media, but also open new pathways for biomass conversion, demonstrating considerable scientific and practical potential.

Author contributions

Guanggang Gao, Yundong Cao and Hong Liu conceived the project and designed the experiments. Lixiao Song performed the experiments and interpreted the data contributions with the assistance of Ziwei Cai, Caili Lv, Longfei Chao, Wenjing Xu and Chunhui Zhang. The manuscript was written by Lixiao Song with insightful discussion and proofreading of Guanggang Gao. All authors have given approval to the final version of the manuscript.

Conflicts of interest

The authors declare no competing financial interest.

Data availability

The data supporting this article have been included as part of the supplementary information (SI). Supplementary information: Tables S1 and S2, FTIR, PXRD, and TEM experimental details. See DOI: https://doi.org/10.1039/d5dt03085d.

Acknowledgements

The authors gratefully acknowledge the financial support from the National Natural Science Foundation of China (22471095), the Jinan City "New University 20" Project (202228113), the Postdoctoral Fellowship Program of CPSF (GZC20250015), the Postdoctoral Innovation Program of Shandong Province (SDCX-ZG-202502050), the Natural Science Foundation of Shandong Province (ZR2024QE440), and the Science and Technology Program of the University of Jinan (XBS2404).

References

1 Q. Liu, J. Shang and Z. Liu, Zeolites in the epoch of catalytic recycling plastic waste: toward circular economy and sustainability, *Chin. J. Catal.*, 2025, **71**, 54–69, DOI: 10.1016/s1872-2067(24)60273-1.
2 Y. Qi, C. J. Lin, Z. Sun, Y. N. Chen, Q. W. Wang, X. H. Wang and X. Z. Duan, Fabricating $Ce(DS)_2H_4AlW_{12}O_{40}$ as a single-cluster heterogeneous catalyst for highly efficient conversion of cellulose to 5-HMF in water and in biphase, *Renewable Energy*, 2025, **255**, 123796, DOI: 10.1016/j.renene.2025.
3 G. Liu, J. Zheng, X. Q. Huang, S. Q. Fu, S. Q. Xi, Y. L. Zhang, Z. Li, F. Yu and Y. F. Chen, One-pot cascade conversion of fructose to 2,5-diformylfuran enabled by a polyionic liquid-based porous catalyst, *Inorg. Chem. Front.*, 2025, **12**, 4703–4711, DOI: 10.1039/D5QI00135H.
4 T. Xia, W. B. Gong, Y. H. Chen, M. L. Duan, J. Ma, X. F. Cui, Y. T. Dai, C. Gao and Y. J. Xiong, Sunlight-driven highly selective catalytic oxidation of 5-hydroxymethylfurfural towards tunable products, *Angew. Chem., Int. Ed.*, 2022, **61**, e202204225, DOI: 10.1002/anie.202204225.
5 Z. H. Hou, Y. F. Wu, W. J. Cao and C. L. Wang, Construction of NiCu heterojunctions for highly efficient and profitable electrooxidation of HMF to FDCA: The indications from techno-economic analysis, *Appl. Catal., B*, 2026, **382**, 125938, DOI: 10.1016/j.apcatb.2025.125938.
6 J. Feng, D. X. Yan, C. R. Rong, L. Z. Yu, J. B. Li, J. Y. Xin, X. M. Lu, Q. Zhou, Z. Q. Wang and Z. Wei, Efficient synthesis of high molecular weight semi-aromatic polyamides with biobased furans over metal-free ionic liquids, *Green Chem.*, 2025, **27**, 3335–3345, DOI: 10.1039/d4gc06245k.
7 B. A. Abel and G. W. Coates, Introduction: the future of plastics sustainability, *Chem. Rev.*, 2025, **125**, 1255–1256, DOI: 10.1021/acs.chemrev.4c00958.
8 Z. X. Ye, Y. L. Liu, W. D. Chem, Z. Yu, Y. J. Fang, X. Y. Zhou, Y. R. He, Y. Wang and Z. B. Tang, Bio-based, closed-loop chemical recyclable aromatic polyamide from 2,5-furandicarboxylic acid: synthesis, high performances, and degradation mechanism, *Eur. Polym. J.*, 2024, **210**, 112935, DOI: 10.1016/j.eurpolymj.2024.112935.
9 A. Corma, S. Iborra and A. Velty, Chemical routes for the transformation of biomass into chemicals, *Chem. Rev.*, 2007, **107**, 2411–2502, DOI: 10.1021/cr050989d.
10 Z. Y. Zhang, X. W. Zhang, S. Y. Qi, Q. Na, K. C. Zhao, Z. Y. Yu, Z. T. Tan, H. J. Ying and C. J. Zhu, Constructing a chemoenzymatic strategy for enhancing the efficiency of selectively transforming 5-hydroxymethylfurfural into furan

carboxylic acids, *Green Chem.*, 2025, **27**, 642–649, DOI: 10.1039/D4GC04735D.

11 Q. Yang, C. Wu, T. Zhang, Y. C. He and C. Ma, Efficient bio-oxidation of biomass-derived furan-2,5-dicarbaldehyde to 5-formyl-2-furoic acid and 2,5-furandicarboxylic acid via whole-cell biocatalysis, *Bioresour. Technol.*, 2025, **421**, 132201, DOI: 10.1016/j.biortech.2025.132201.

12 S. F. Yu, C. H. Song, H. W. Zhang, W. P. Liao, D. Y. Zhao, C. Len, H. Y. Lü and T. Su, One-step hydrothermal fabrication of visible-light-responsive pompon-like $SnxInyS_{2x+1.5y}$ heterojunctions for highly-efficient photocatalytic oxidation of 5-hydroxymethylfurfural without additional oxidants, *J. Alloys Compd.*, 2024, **982**, 173810, DOI: 10.1016/j.jallcom.2024.173810.

13 C. L. Wang, Z. Y. Zhao, W. J. Cao, Y. J. Peng, M. W. Song and Y. F. Wu, A metal–free carbonaceous material for highly efficient and robust electrochemical biomass valorization, *Adv. Funct. Mater.*, 2025, **35**, 2502618, DOI: 10.1002/adfm.202502618.

14 Z. Y. Gao, M. Y. Wang, N. Z. Shang, W. Gao, X. Cheng, S. T. Gao, Y. J. Gao and C. Wang, Highly dispersed Co anchored on Ce-doped hydroxyapatite as a dual-functional catalyst for selective hydrogenolysis of 5-hydroxymethylfurfural, *Dalton Trans.*, 2023, **52**, 11076–11084, DOI: 10.1016/j.cej.2025.161520.

15 P. A. Son, S. Nishimura and K. Ebitani, Synthesis of levulinic acid from fructose using Amberlyst-15 as a solid acid catalyst, *React. Kinet., Mech. Catal.*, 2012, **106**, 185–192, DOI: 10.1007/s11144-012-0429-1.

16 Q. G. Hou, T. Y. Gao, H. Zhang, Q. H. Tang and W. H. Fang, Pt nanoparticles in cooperation with Mn-P composite drive base-free selective oxidation of 5-hydroxymethylfurfural, *Catal. Today*, 2025, **443**, 114990, DOI: 10.1016/j.cattod.2024.114990.

17 M. K. Ke, Y. Min, S. C. Mei, H. W. Zeng, Z. H. Wang, T. W. Hua, J. J. Chen, G. X. Huang and H. Q. Yu, Highly selective oxidation of 5-HMF to HMFCA via a facile Pt-Ag co-catalytic strategy, *Appl. Catal., B*, 2024, **358**, 124431, DOI: 10.1016/j.apcatb.2024.124431.

18 J. T. Zhang, Y. Yang, G. X. Ding, Z. Q. Wang, P. Wang, C. X. Li and G. F. Liao, Electrooxidation of biomass-derived 5-hydroxymethylfurfural over sulfur-doped nickel-iron layered double hydroxides nanosheets, *Chem. Eng. J.*, 2025, **505**, 159165, DOI: 10.1016/j.cej.2024.159165.

19 P. Rapado, C. Lois, M. Cano, L. Faba and S. Ordóñez, Biomass to plastics: from HMF to fructose for the synthesis of 2,5-furandicarboxylic acid over Au/TiO_2, *Catal. Today*, 2025, **445**, 115036, DOI: 10.1016/j.cattod.2024.115036.

20 E. J. D. Boed, H. L. Nolten, N. Masoud, R. Vogel, F. Wang, Z. Xu, E. J. Doskocil, B. Donoeva and P. E. D. Jongh, Effect of Ag addition to Au catalysts for the oxidation of 5-hydroxymethylfurfural to 2,5-furandicarboxylic acid, *ChemCatChem*, 2024, **16**, e202301436, DOI: 10.1002/cctc.202301436.

21 S. Somsri, A. Prasertsab, P. Pornsetmetakul, N. Maineawklang, M. T. Nguyen, T. Yonezawa and C. Wattanakit, Synthesis of cyclodextrin-stabilized gold nanoparticles supported hierarchical zeolites for the facile production of furandicarboxylic acid (FDCA) from 5-hydroxymethylfurfural (HMF), *Microporous Mesoporous Mater.*, 2023, **354**, 112559, DOI: 10.1016/j.micromeso.2023.112559.

22 B. K. Chen, Y. Y. Abe, H. X. Duo and R. L. Smith, Selective oxidation of 5-hydroxymethylfurfural over MnO_x-CeO_2 catalyst prepared with co-precipitation method, *Fuel*, 2024, **376**, 132745, DOI: 10.1016/j.fuel.2024.132745.

23 Y. Li, Y. Shen, J. Zhang, C. Chen, X. Zhang, B. Y. Geng and G. Z. Wang, Sustainable production of bio-based pentanediol from ring-opening hydrogenolysis of furan derivative over hydrotalcite-derived mixed metal oxide catalyst, *Fuel*, 2025, **387**, 134398, DOI: 10.1016/j.fuel.2025.134398.

24 Y. N. Peng, X. Y. Zhou, X. Z. Liu, M. Hu, B. Y. Qiu, Y. L. Jiao, C. Agostino, J. Esteban, C. M. A. Parlett and X. L. Fan, To alloy or not to alloy? The unexpected power of Pd-Au catalyst physical mixtures in efficient HMF oxidation to FDCA, *ACS Catal.*, 2025, **15**, 11760–11773, DOI: 10.1021/acscatal.5c02908.

25 Y. Ruan, S. Y. Wu, Y. Lu, T. f. Xu, W. X. Chen and W. Y. Lü, Bidirectional S-bridge coordination in the magnetic Au/FeO_xS_y catalyst for the catalytic oxidation of 5-hydroxymethylfurfural to 2,5-furandicarboxylic acid, *J. Mater. Chem. A*, 2025, **13**, 10814–10824, DOI: 10.1039/D4TA09277E.

26 J. R. Li, R. X. Qiu, S. W. Zhang, L. Peng, Y. Y. Dong, Y. Jiang, Y. Li, N. Fang, J. Yu, J. C. Dong, H. H. Zheng, L. Z. Ding, J. L. Wan, I. Akpinar, J. H. Kuang, G. F. Chen, J. Y. Ye, Y. Sun, L. Lin, S. S. Zheng, S. L. Yang, J. Li and J. F. Li, Synergistically enhanced co-adsorption of reactant and hydroxyl on platinum-modified copper oxide for high-performance HMF oxidation, *Adv. Mater.*, 2025, **37**, 2417684, DOI: 10.1002/adma.202417684.

27 W. Z. Yang, Y. J. Liu, M. Y. Wang, X. Y. Wang, Q. D. Liu, L. J. Lan, P. C. Yin, C. H. Zhan, Z. G. Jiang and X. Wang, Giant five-shell polyoxometalate cages and the single-cluster-based nanowire superstructures, *J. Am. Chem. Soc.*, 2025, **147**, 25990–25997, DOI: 10.1021/jacs.5c08771.

28 R. Z. Sun, X. Ma, K. Chen, J. B. Yang, Y. X. Liu, X. X. Li, P. W. Cai, Z. H. Wen and S. T. Zheng, Self-assembled polyoxometalate supramolecular nanosheets for efficient and durable water oxidation, *Angew. Chem., Int. Ed.*, 2025, **64**, e202513915, DOI: 10.1002/anie.202513915.

29 X. D. Xie, J. J. Liu, J. M. Lin, N. Li, X. H. Chen, X. Y. Lin, Y. T. Hao, S. L. Li, J. Liu and Y. Q. Lan, Hollow giant polyoxometalate oxidation shell encapsulating molecular reduction core for unprecedented photoredox cascade conversion, *Chem*, 2025, **11**, 102572, DOI: 10.1016/j.chempr.2025.102572.

30 L. P. Cui, S. Zhang, Y. Zhao, X. Y. Ge, L. Yang, K. Li, L. B. Feng, R. G. Li and J. J. Chen, Tunable multi-electron redox polyoxometalates for decoupled water splitting driven by sunlight, *Nat. Commun.*, 2025, **16**, 3674, DOI: 10.1038/s41467-025-58622-8.

31 H. P. Xiao, Y. S. Hao, X. X. Li, P. Xu, M. D. Huang and S. T. Zheng, A water-soluble antimony-rich polyoxometalate with broad-spectrum antitumor activities, *Angew. Chem., Int. Ed.*, 2022, **61**, e202210019, DOI: 10.1002/anie.202210019.

32 A. Magerat, S. Hermans and E. Gaigneaux, A novel versatile platform as efficient deoxydehydration (DODH) catalysts: Keggin polyoxometalates, *Appl. Catal., B*, 2025, **375**, 125432, DOI: 10.1016/j.apcatb.2025.125432.

33 X. Zhang, X. C. Lv, X. Du, M. H. Qi, S. J. Mao and Y. Wang, High-temperature-mediated assembly of polyoxometalate-induced ordered carbonaceous superstructures, *Angew. Chem., Int. Ed.*, 2024, **64**, e202423242, DOI: 10.1002/anie.202423242.

34 F. H. Zhang, H. Y. Li, Z. Li, Q. D. Liu and X. Wang, Phase engineering of polyoxometalate assembled superstructures, *Nat. Synth.*, 2024, **3**, 1039–1048, DOI: 10.1038/s44160-024-00569-7.

35 M. Pascual-Borràs, E. Arca, H. Yoshikawa, T. Penfold, P. G. Waddell and R. J. Errington, Mechanochemical polyoxometalate super-reduction with lithium metal, *J. Am. Chem. Soc.*, 2024, **146**, 26485–26496, DOI: 10.1021/jacs.4c09998.

36 A. Ebrahimi, L. Krivosudský, A. Cherevan and D. Eder, Polyoxometalate-based porphyrinic metal-organic frameworks as heterogeneous catalysts, *Coord. Chem. Rev.*, 2024, **508**, 215764, DOI: 10.1016/j.ccr.2024.215764.

37 T. Ma, R. Yan, X. Z. Wu, M. Wang, B. Yin, S. Li, C. Cheng and A. Thomas, Polyoxometalate-structured materials: molecular fundamentals and electrocatalytic roles in energy conversion, *Adv. Mater.*, 2024, **36**, 2310283, DOI: 10.1002/adma.202310283.

38 R. Y. Zhou, Y. Liao, H. Z. Xu, Z. J. Gu and Z. W. Leng, Polyoxometalates: versatile nanomedicine candidates for precise cancer therapy, *Chem. Eng. J.*, 2025, **512**, 162335, DOI: 10.1016/j.cej.2025.162335.

39 M. M. Ma, Z. Q. Liu, H. S. Zhao, H. C. Zhang, J. S. Ren and X. G. Qu, Polyoxometalates: metallodrug agents for combating amyloid aggregation, *Natl. Sci. Rev.*, 2024, **11**, nwae226, DOI: 10.1093/nsr/nwae226.

40 H. H. Yu, J. B. Huang, J. Xu, H. Z. Liu, Y. T. Zhang, Z. Sun, L. Yang, X. H. Guan and L. Kong, Electron spin polarization promotes photocatalytic hydrogen production: assembly of polyoxometalate-based magnetic-responsable heterojunction and magnetic modulation mechanism, *Appl. Surf. Sci.*, 2025, **707**, 163650, DOI: 10.1016/j.apsusc.2025.163650.

41 H. Song, M. S. Gou, J. F. Wang, Y. Q. Liu, H. X. Bi, J. Du, W. T. An, Y. Y. Ma and Z. G. Han, Reduced phosphomolybdate as photoassisted electrochemical crystalline sensor for trace Cr(VI) detection, *Polyoxometalates*, 2024, **3**, 9140065, DOI: 10.26599/POM.2024.9140065.

42 T. T. Gong, S. Wang, Y. N. Chen, L. J. Chen and J. W. Zhao, Tetrahydroxyhexanedioic acid-ornamented phosphite-and-bismuth-bridging EuIII-encapsulated phospho(III)tungstate and its photochromic and photoluminescence switching properties, *ACS Appl. Mater. Interfaces*, 2025, **17**, 63642–63651, DOI: 10.1021/acsami.5c19350.

43 C. H. Zhang, J. Wang, J. Y. Zhan, R. M. Yang, G. G. Gao, J. Y. Zhang, L. L. Fan, M. Q. Wang and H. Liu, Highly sensitive hydrazine detection through a novel raman scattering quenching mechanism enabled by a crystalline and noble metal-free polyoxometalate substrate, *Chin. Chem. Lett.*, 2025, **36**, 109719, DOI: 10.1016/j.cclet.2024.109719.

44 J. Wang, J. Y. Zhang, W. J. Zhu, B. Qi, J. P. Wang, G. G. Gao, L. L. Fan and H. Liu, Ratiometric SERS detection of N_2H_4 by porous Ag(I)-linked waugh-type polyoxometalate as an efficient label-free substrate, *J. Mater. Chem. C*, 2023, **11**, 3050–3058, DOI: 10.1039/D2TC05148F.

45 J. Wang, W. J. Zhu, J. Y. Zhang, B. Qi, J. P. Wang, G. G. Gao, L. L. Fan and H. Liu, Ratiometric response to formaldehyde by 3D silver SERS substrate with polyoxometalate as internal label, *Sens. Actuators, B*, 2023, **381**, 133450, DOI: 10.1016/j.snb.2023.133450.

46 J. Y. Zhang, X. Y. Zhang, J. Wang, Y. Feng, L. L. Fan, Y. D. Cao, H. Liu, C. L. Lv and G. G. Gao, The explicit multi–electron catalytic mechanism of heteropolyvanadotungstate dominating ultra–durable room–temperature Na–S batteries, *Adv. Funct. Mater.*, 2024, **34**, 2400170, DOI: 10.1002/adfm.202400170.

47 Y. H. Song, J. Y. Zhang, C. H. Zhang, L. L. Fan, J. Song, Y. D. Cao, Y. Feng, H. Liu and G. G. Gao, Constructing artificial interphase layer of polyoxovanadates with high oxidizability and reversibility to boost dendrite-free lithium metal anode, *Chem. Eng. J.*, 2025, **519**, 165237, DOI: 10.1016/j.cej.2025.165237.

48 C. L. Lv, Y. D. Cao, Y. Feng, L. L. Fan, J. Y. Zhang, Y. H. Song, H. Liu and G. G. Gao, Crosslinked vinyl-capped polyoxometalates to construct a three-dimensional porous inorganic-organic catalyst to effectively suppress polysulfide shuttle in Li-S batteries, *Adv. Energy Mater.*, 2025, e05978, DOI: 10.1002/aenm.202505978.

49 C. H. Zhang, M. Q. Wang, C. H. Zhao, J. P. Wang, Y. D. Cao, L. L. Fan, H. Liu and G. G. Gao, Enhanced selective oxidation of 5-hydroxymethylfurfural with a recyclable V_{34}@Fe_3O_4/C catalyst enriched with mixed-valence polyoxovanadate active centers, *Fuel*, 2025, **397**, 135439, DOI: 10.1016/j.fuel.2025.135439.

50 Y. D. Cao, W. X. Mu, M. D. Gong, L. L. Fan, J. Han, H. Liu, B. Qi and G. G. Gao, Enhanced catalysis of a vanadium-substituted Keggin-type polyoxomolybdate supported on the M_3O_4/C (M = Fe or Co) surface enables efficient and recyclable oxidation of HMF to DFF, *Dalton Trans.*, 2023, **52**, 16303–16314, DOI: 10.1039/D3DT02935B.

51 M. D. Gong, W. X. Mu, Y. D. Cao, Y. W. Shao, X. Hu, D. Yin, H. Liu, C. H. Zhang and G. G. Gao, A giant polyoxomolybdate molecular catalyst with unusual Mo^{6+}/Mo^{5+} synergistic mechanism for oxidation of hydroxyfurfural under atmospheric pressure, *Fuel Process. Technol.*, 2023, **242**, 107635, DOI: 10.1016/j.fuproc.2022.107635.

52 M. D. Gong, X. Y. Wang, M. Q. Li, W. X. Mu, Y. D. Cao, H. Liu, Y. G. Lv, X. H. Qi and G. G. Gao, High-efficient and

recoverable $Mo_{72}V_{30}$@Fe_3O_4/C catalyst for oxidation of hydroxyfurfural, *Fuel*, 2023, **332**, 126050, DOI: 10.1016/j.fuel.2022.126050.

53 R. R. Chen, J. Y. Xin, D. X. Yan, H. X. Dong, X. M. Lu and S. J. Zhang, Highly efficient oxidation of 5-hydroxymethylfurfural to 2,5-furandicarboxylic acid with heteropoly acids and ionic liquids, *ChemSusChem*, 2019, **12**, 2715–2724, DOI: 10.1002/cssc.201900651.

54 S. Li, K. M. Su, Z. H. Li and B. Cheng, Selective oxidation of 5-hydroxymethylfurfural with H_2O_2 catalyzed by a molybdenum complex, *Green Chem.*, 2016, **18**, 2122–2128, DOI: 10.1039/C5GC01991E.

55 H. P. Xiao, M. Y. Du, X. B. Sun, R. F. Xu, D. M. Li, S. N. Yue, P. W. Cai, R. Z. Sun, Z. Z. Zhang, X. Huang, X. X. Li, Y. Gao and S. T. Zheng, A highly biocompatible polyoxotungstate with fenton-like reaction activity for potent chemodynamic therapy of tumors, *Angew. Chem., Int. Ed.*, 2024, **64**, e202422949, DOI: 10.1002/anie.202422949.

56 Y. X. Liu, P. X. Wu, J. Y. Dai, P. W. Cai, C. Sun and S. T. Zheng, Site differentiation strategy for selective strontium uptake and elution within an all-inorganic polyoxoniobate framework, *Nat. Commun.*, 2024, **15**, 8896, DOI: 10.1038/s41467-024-53130-7.

57 Y. R. Li, C. X. Chen, K. H. Qi, C. Sun and S. T. Zheng, Development of an integrated polyoxoniobate with oxygen activation and basicity as green catalyst for efficient aerobic oxidation of aldehydes at room temperature, *Green Chem.*, 2025, **27**, 7781–7787, DOI: 10.1039/D5GC01576F.

58 Z. W. Guo, L. H. Lin, J. P. Ye, Y. Chen, X. X. Li, S. Lin, J. D. Huang and S. T. Zheng, Core–shell–type all–inorganic heterometallic nanoclusters: record high–nuclearity cobalt polyoxoniobates for visible–light–driven photocatalytic CO_2 reduction, *Angew. Chem.*, 2023, **135**, e202305260, DOI: 10.1002/ange.202305260.

59 H. F. Liu, X. R. Sun, J. Dong, C. P. Liu, W. Lu, Z. M. Xu, N. Zhen, D. Zhang, Y. N. Chi and C. W. Hu, Immobilization of Bronsted basic hexaniobate on the Lewis acidic zirconia using an emulsion assisted self-assembly strategy for synergistic boosting of nerve agent simulant decontamination, *Inorg. Chem. Front.*, 2023, **10**, 1436–1446, DOI: 10.1039/D2QI02484E.

60 C. X. Chen, S. L. Duan, X. Y. Zhang, R. Z. Sun, P. W. Cai, C. Sun and S. T. Zheng, Organic-inorganic hybrid Co-containing polyoxoniobates as hydrogen evolution catalysts in alkaline media, *Dalton Trans.*, 2025, **54**, 3591–3596, DOI: 10.1039/D4DT03071K.

61 J. Li, P. P. Shao, W. J. Geng, P. Lei, J. Dong, Y. N. Chi and C. W. Hu, Highly efficient oxidative cleavage of lignin b-O-4 linkages via synergistic Co-CoO_x/N-doped carbon and recyclable hexaniobate catalysis, *Green Chem.*, 2025, **27**, 827–837, DOI: 10.1039/D4GC05120C.

62 J. Li, Z. Li, J. Dong, R. B. Fang, Y. N. Chi and C. W. Hu, Hexaniobate as a recyclable solid base catalyst to activate C-H bonds in lignin linkage boosting the production of aromatic monomers, *ACS Catal.*, 2023, **13**, 5272–5284, DOI: 10.1021/acscatal.2c06206.

63 G. L. Gou, Y. Q. Xu, J. Cao and C. W. Hu, An unprecedented vanadoniobate cluster with 'trans-vanadium' bicapped Keggin-type $\{VNb_{12}O_{40}(VO)_2\}$, *Chem. Commun.*, 2011, **47**, 9411–9413, DOI: 10.1039/C1CC12329G.

64 S. D. McCann and S. S. Stahl, Mechanism of copper/azodicarboxylate-catalyzed aerobic alcohol oxidation: evidence for uncooperative catalysis, *J. Am. Chem. Soc.*, 2016, **138**, 199–206, DOI: 10.1021/jacs.5b09940.

65 J. M. Molinaro, M. R. Carroll, A. S. Young and S. G. Wettstein, Solubility of 2,5-furandicarboxylic acid in pure and mixed organic solvent systems at 293 K predicted using hansen solubility parameters, *ACS Omega*, 2024, **9**, 30708–30716, DOI: 10.1021/acsomega.4c03170.

66 Y. J. Pang, N. Chen, Z. Z. Zhao, L. Zhang, J. O. P. Broekman, J. N. Wei, X. J. Li, L. Lin and H. Huang, A unique air-assisted DMSO oxidation pathway for the highly efficient synthesis of 2,5-diformylfuran from 5-hydroxymethylfurfural/fructose, *Green Chem.*, 2023, **25**, 9680–9688, DOI: 10.1039/D3GC02279J.

67 B. Yang, W. W. Hu, F. F. Wan, C. Zhang, Z. H. Fu, A. Q. Su, M. K. Chen and Y. C. Liu, Adjusting effect of additives on decatungstate-photocatalyzed HMF oxidation with molecular oxygen under visible light illumination, *Chem. Eng. J.*, 2020, **396**, 125345, DOI: 10.1016/j.cej.2020.125345.

68 G. D. Yadav and R. V. Sharma, Biomass derived chemicals: environmentally benign process for oxidation of 5-hydroxymethylfurfural to 2,5-diformylfuran by using nano-fibrous Ag-OMS-2-catalyst, *Appl. Catal., B*, 2014, **147**, 293–301, DOI: 10.1016/j.apcatb.2013.09.004.

69 T. H. Nguyen, D. A. L. Nguyen, D. Q. Mai, M. N. T. Le, D. D. Le and P. H. Tran, Cobalt-modified nitrogen-doped carbon nanotubes as bifunctional catalysts for one-pot synthesis of 2,5-diformylfuran from glucose, *J. Energy Chem.*, 2025, **103**, 440–447, DOI: 10.1016/j.jechem.2024.11.074.

70 D. Gao, F. Y. Fang, G. I. N. Waterhouse, F. Han and Y. Li, S, P modified CoFe-LDH derived CoFeS and CoFeP-400 catalysts efficiently catalyze the oxidation of HMF to FDCA, *Catal. Sci. Technol.*, 2024, **14**, 1191–1200, DOI: 10.1039/D4CY00010B.

71 H. L. Qian, K. Y. Zhang, Y. C. He, Q. D. Hou, C. Xie, R. T. Lai, G. J. Yu, T. L. Xia, X. Y. Bai, H. J. Xie and M. T. Ju, Engineering crystal plane of $NiCo_2O_4$ to regulate oxygen vacancies and acid sites for alkali-free oxidation of 5-hydroxymethylfurfural to 2,5-furandicarboxylic acid, *Green Energy Environ.*, 2025, **10**, 756–765, DOI: 10.1016/j.gee.2024.05.002.

72 X. Gao, Z. H. Li, S. X. Zhang, D. S. Zhang, X. Q. Zhao, B. Q. Zhang and Y. J. Wang, Advancements in biomass conversion: copper-catalyzed anaerobic dehydrogenation of 5-hydroxymethylfurfural to 2,5-diformylfuran, *Chem. Eng. J.*, 2024, **496**, 153775, DOI: 10.1016/j.cej.2024.153775.

